Optical Engineering

OpticalEngineering.SPIEDigitalLibrary.org

Automatic registration of fused lidar/digital imagery (texel images) for three-dimensional image creation

Scott E. Budge
Neeraj S. Badamikar
Xuan Xie

SPIE.

Automatic registration of fused lidar/digital imagery (texel images) for three-dimensional image creation

Scott E. Budge,* Neeraj S. Badamikar, and Xuan Xie
Utah State University, Center for Advanced Imaging Ladar, Department of Electrical and Computer Engineering, 4120 Old Main Hill, Logan, Utah 84322-4120, United States

Abstract. Several photogrammetry-based methods have been proposed that the derive three-dimensional (3-D) information from digital images from different perspectives, and lidar-based methods have been proposed that merge lidar point clouds and texture the merged point clouds with digital imagery. Image registration alone has difficulty with smooth regions with low contrast, whereas point cloud merging alone has difficulty with outliers and a lack of proper convergence in the merging process. This paper presents a method to create 3-D images that uses the unique properties of texel images (pixel-fused lidar and digital imagery) to improve the quality and robustness of fused 3-D images. The proposed method uses both image processing and point-cloud merging to combine texel images in an iterative technique. Since the digital image pixels and the lidar 3-D points are fused at the sensor level, more accurate 3-D images are generated because registration of image data automatically improves the merging of the point clouds, and vice versa. Examples illustrate the value of this method over other methods. The proposed method also includes modifications for the situation where an estimate of position and attitude of the sensor is known, when obtained from low-cost global positioning systems and inertial measurement units sensors. [DOI: 10.1117/1.OE.54.3.031105]

Keywords: lidar; ladar; three-dimensional image creation; texel image; image registration; image and lidar fusion; point cloud matching.

Paper 141028SSP received Jun. 30, 2014; revised manuscript received Sep. 27, 2014; accepted for publication Oct. 7, 2014; published online Nov. 6, 2014.

1 Introduction

Generation of three-dimensional (3-D) imagery is a topic of interest in many applications. These datasets result from texturing a 3-D surface with digital imagery, resulting in a 3-D image made up of textured elements, or "texels," a term used in computer graphics literature. The 3-D images can then be used to create models of historical sites, document archaeological artifacts, or document topography. On a smaller scale, 3-D images can be used for object recognition in defense and surveillance applications, such as targeting, monitoring, person identification, or people counting.[1]

There have been many efforts to create datasets that include both 3-D sensed data and imagery from a scene. These include hardware configuration methods, such as combining stereo camera pairs with a lidar sensor,[2–4] methods based on edges, geometric features, or match points,[5–9] methods based in optical flow,[10] or methods based on mutual information.[11]

There have also been many efforts to match two-dimensional (2-D) datasets and create 3-D models from the images. Many of the 2-D methods are based in the well-known mathematics of projective geometry and stereo pairs.[12–14] Although often effective, these methods are not robust in some practical situations. In addition, a significant amount of computation is required to construct the 3-D surface. A good tutorial on image registration is given by Zitova and Flusser.[15]

A significant problem in 2-D image registration is automatically finding corresponding feature points using correlation. When the perspectives between images are widely separated, perspective distortion in the images causes the correlation between true correspondences to decrease to the point where correlation thresholds are not robust. Several authors have proposed methods to address this problem in matching feature points in imagery. These methods can be generally classed as affine-invariant methods,[16,17] scale-invariant methods,[18,19] or other feature-based methods.[20,21] As proposed in a preliminary work,[22] coarse position and attitude knowledge from low-cost global positioning systems and inertial measurement units (GPS/IMU) can be used to avoid correlation.

Other efforts have been made in matching 3-D datasets. The seminal work of Besl and McKay[23] in developing an iterative method for matching 3-D point clouds has led to various improvements for the performance of the basic algorithm.[24,25] Other 3-D methods have been developed that are guided by lidar intensity data.[26]

The goal of this work is to present a method that uses previously fused imagery and lidar data to register 3-D textured surfaces. If the datasets are taken from different perspectives around a 3-D scene, the registered datasets will produce a true 3-D image of the scene. Since the datasets contain fused 2-D and 3-D data, both 2-D and 3-D registration methods can be employed to better register the datasets.[27]

The remainder of the paper proceeds as follows. Section 2 begins by describing the combined sensor used in this work. Section 3 describes the basic method used to register the datasets based on both the 2-D digital imagery and the 3-D lidar data contained in texel images, followed by Sec. 4, which describes modifications when coarse GPS/IMU data

*Address all correspondence to: Scott E. Budge, E-mail: scott.budge@ece.usu.edu

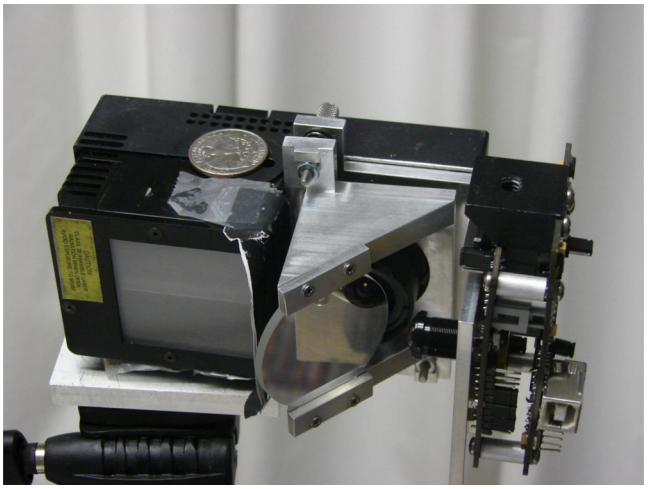

Fig. 1 Texel camera constructed from a time-of-flight depth sensor and an imaging [electro-optic (EO)] sensor.

are known. Finally, registration results are given in Sec. 5, and Sec. 6 concludes the paper.

2 Texel Camera

The combination of a flash or time-of-flight lidar with a digital (electro-optic or EO) camera that produces data that is fused at the subpixel level is known as a "texel camera.[28–30]" An example of a compact texel camera prototype is shown in Fig. 1, with sensor specifications given in Table 1. Additional details are given in the literature.[31] The camera is constructed to directly produce fused datasets—no post processing is necessary. This is possible because each 3-D lidar measurement obtained from the lidar sensor array is assigned, through a calibration process, to a pixel in the simultaneously captured EO image.[31] The EO pixel assigned to each lidar measurement is the projection of the 3-D lidar point onto the EO image. This assignment is given as the set $\{\boldsymbol{x}:\boldsymbol{x}\rightarrow\boldsymbol{u}\}$, where $\boldsymbol{x}$ is a 3-D lidar point and $\boldsymbol{u}$ is a corresponding 2-D point in the EO image.

Direct sensing of a 3-D surface using lidar imaging can be used to create a triangulated interconnected network (TIN or wireframe model) to represent the surface. This surface can then be textured with a digital (EO) image of the surface, creating a "texel image." The texel image is, therefore, a fused dataset, where the spatial resolution of the image pixels is higher than the resolution of the lidar sensor. An additional advantage of these datasets is that there is no misregistration due to sensor motion.

Since the resolution of the EO sensor is much higher than the resolution of the lidar sensor, only a few of the EO pixels correspond directly to projected 3-D points measured by the lidar. As a result, other pixels in the EO image must be assigned 3-D points by interpolation of the lidar pixels fused to the surrounding EO pixels. When correctly calibrated, there is a one-to-one correspondence between 3-D points in the sensor field-of-view and the pixels in the EO image. This means that a 3-D point, referenced to the center of projection (COP) of the lidar sensor, is assigned to each pixel in the EO image.

An example of a dataset produced by a texel camera is given in Fig. 2.

Table 1 Specifications for prototype texel camera.

Specifications	
Lidar array size	64×64 pixels
EO array size	1280×1024 pixels
Calibrated range	0.2 to 2.1 m
Calibrated range error $(1-\sigma)$	<3 mm

3 Image Registration Using Texel Images

The creation of 3-D images results from the registration of several texel images acquired from different viewpoints around the 3-D object of interest. If each position and attitude of a texel camera is known to a high degree of accuracy in a common frame of reference, it is possible to immediately register the images, and the overlapping areas of the texel images can be combined to create a continuous textured surface. It is of interest, however, to create fused images without the cost of a highly accurate position/attitude measurement system.

The fused nature of texel images allow registration methods that exploit the EO image data or the 3-D lidar data, or both, when the situation requires it. If the EO images contain few features or smooth areas, it is difficult to find correspondences and compute 3-D information using machine vision approaches (In theory, at least eight correspondences are needed,[13] but in practice five times that many may be necessary for a good registration.). If the overlapping 3-D points alone are used to register the 3-D surfaces, the well-known iterated closest point (ICP) algorithms may diverge due to outliers and noise.[23,25] The initial approach taken in this paper is to use image features as a starting point, and then exploit the 3-D information associated with each EO pixel to find the 3-D transformation to register the texel images. No *a priori* information about the position and attitude of the texel camera is known. This requires that there will be an overlap in the images that contains a set of corresponding feature points $(\boldsymbol{u},\boldsymbol{u}')$, where $\boldsymbol{u}$ is a point in the first image, and $\boldsymbol{u}'$ is a point in the second image.

Algorithm 1 summarizes the steps for registering texel images acquired from arbitrary overlapping perspectives. Note that steps 1 to 4 of the algorithm exploit the 2-D EO information, and steps 5 to 7 exploit the 3-D lidar information in the texel image. The end result of the algorithm is an estimate of the 3-D rotation matrix, $\hat{\boldsymbol{R}}$, and translation vector, $\hat{\boldsymbol{t}}$, describing the coordinate transformation from the second texel image frame into the first texel image frame.

During the process of finding point correspondences, it is possible to find many points in one image that possibly correspond to one point in the other image. This is denoted as the set $\{(\boldsymbol{u},\boldsymbol{u}_s')\}$, where there are s features in image 2 that correspond to a feature in image 1.

3.1 *Detecting Harris Features*

The first step in the basic algorithm is to detect Harris features[32] in each of the EO images. These are points that occur at corners and are detected as points that have large curvatures in both principal directions. Since the

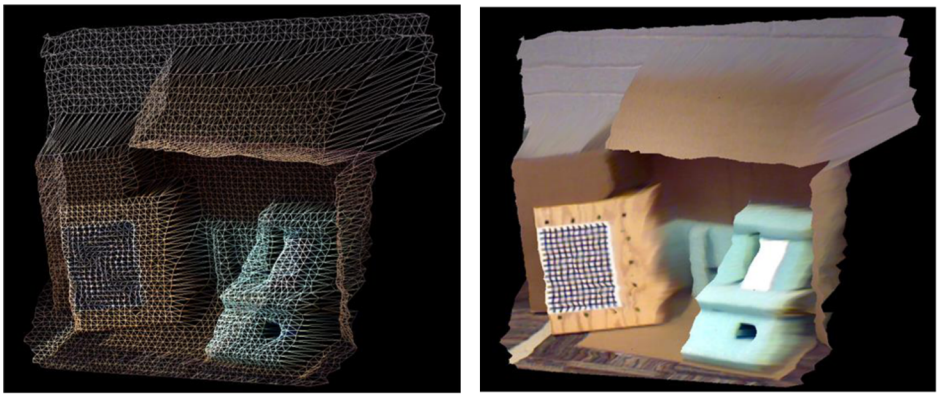

(a) (b)

Fig. 2 Examples of a texel image. (a) Triangulated, interconnected network (TIN) created from the lidar measurements. (b) Textured TIN surface, or texel image.

EO images are color, each of the color planes are processed individually, and the detected points from each of the planes are added to a list of feature points. Examples of feature points found in a pair of overlapping EO images are given in Fig. 3.

In order to reduce the effect of illumination on the ability to detect features, the Harris features were detected in the YCrCb color space. Detections are independently made on all three color planes.

3.2 *Finding Putative Correspondences*

The next step of the process is to find features in each EO image that possibly correspond to the same point in the 3-D field-of-view. An assumption is made that the two views overlap and that the corresponding feature points have a high image correlation.

A window is centered on each feature, and the correlation between each of the features in the first image and each of the features in the second image is computed using

$$\gamma_{i,j} = \frac{\sum_{k=-N}^{N}\sum_{l=-N}^{N}[\boldsymbol{u}_i(k,l)-\mu_i][\boldsymbol{u}'_j(k,l)-\mu_j]}{\{\sum_{k=-N}^{N}\sum_{l=-N}^{N}[\boldsymbol{u}_i(k,l)-\mu_i]^2\}^{\frac{1}{2}}\{\sum_{k=-N}^{N}\sum_{l=-N}^{N}[\boldsymbol{u}'_j(k,l)-\mu_j]^2\}^{\frac{1}{2}}}, \tag{1}$$

where the window size is $2N+1$, (k,l) index points in the windows centered about the feature points $\boldsymbol{u}_i$ and $\boldsymbol{u}'_j$, μ_i and μ_j are the mean intensities in the windows, and $\boldsymbol{u}_i(k,l)$ and $\boldsymbol{u}'_j(k,l)$ are the intensities of the pixels in the window around the i'th and j'th feature points in the respective images. If $\gamma_{i,j}$ exceeds a threshold, the features are labeled as putative correspondences. A typical correlation threshold for accepting a correspondence is 0.87. An example of the resulting matches is given in Fig. 4.

3.3 *Random Sample Consensus (RANSAC)*

Once the putative correspondences have been determined, it is necessary to eliminate as many incorrect correspondences (outliers) as possible. A well-known method for eliminating outliers is to use the RANSAC algorithm.[33] RANSAC requires that a model must be used to separate inliers from outliers. This can be done by using a model that imposes a second constraint on the correspondences: they must satisfy the well-known epipolar constraint of projective geometry.[13] For this constraint to hold, the EO images must be calibrated to remove nonlinear distortion.[31]

A geometric interpretation of the constraint is illustrated in Fig. 5, where the 3-D points (red and black) are shown in the image 1 coordinate frame. Any 3-D point $\boldsymbol{x}$ visible in two images will project a point onto the image planes (given by $\boldsymbol{u}$ and $\boldsymbol{u}'$ in the figure). The plane formed by $\boldsymbol{x}$ and the COPs of the two cameras, $\boldsymbol{C}$ and $\boldsymbol{C}'$ (the epipolar plane), must contain the projected points. Therefore, if a putative correspondence does not meet this constraint, it is not a correct correspondence. More precisely, the test for the epipolar constraint is given by

$$\boldsymbol{u}'^{T}\boldsymbol{F}\boldsymbol{u} = 0, \tag{2}$$

where $\boldsymbol{F}$ is the fundamental matrix, and $\boldsymbol{u}$ and $\boldsymbol{u}'$ are in homogeneous coordinates. Note that the epipolar constraint is necessary but not sufficient to determine corresponding points. Any 3-D point that projects to a 2-D point on the epipolar line will meet the constraint. This is illustrated in Fig. 5, where incorrect image correspondences (shown in red) meet the epipolar constraint. The fundamental matrix can be computed from as few as eight correspondences, but is often computed from many more using least-squares (LS) estimation techniques.[34,35] Instead of directly computing Eq. (2), the distance from each correspondence to its epipolar line is computed using the Sampson distance, given by[13]

Algorithm 1 Automatic registration of texel images.

1. Detect Harris features.
2. Determine putative correspondences by 2-D image correlation around features.
3. RANSAC using a fundamental matrix model and the epipolar constraint.
4. Estimate the optimal fundamental matrix $\hat{\boldsymbol{F}}$ and determine putative correspondences that meet the epipolar constraint to within a threshold.
5. Match point clouds using fused EO image/lidar data to create an estimate of the registration transformation $(\hat{\boldsymbol{R}}, \hat{\boldsymbol{t}})$.
6. Use the current estimate $(\hat{\boldsymbol{R}}, \hat{\boldsymbol{t}})$ and the fused EO image/lidar data to test putative correspondences and eliminate incorrect and many-to-one correspondences:
   (a) Estimate the fundamental matrix from $(\hat{\boldsymbol{R}}, \hat{\boldsymbol{t}})$.
   (b) Test each potential correspondence to determine that (3) holds.
   (c) If true, test that the Mahalanobis distance [Eq. (10)] between the corresponding 3-D points $\{(\boldsymbol{x}, \hat{\boldsymbol{x}}_s)\}$ is below a threshold. If all s in the set have a distance greater than the threshold, discard the set $\{(\boldsymbol{u}, \boldsymbol{u}'_s)\}$.
   (d) Select the correspondence with the minimum Euclidean distance out of the set of s correspondences.
7. Repeat step 5.

$$d_S(\boldsymbol{u}, \boldsymbol{u}) = \frac{(\boldsymbol{u}'^T \hat{\boldsymbol{F}} \boldsymbol{u})^2}{(\hat{\boldsymbol{F}}\boldsymbol{u})_1^2 + (\hat{\boldsymbol{F}}\boldsymbol{u})_2^2 + (\hat{\boldsymbol{F}}^T\boldsymbol{u}')_1^2 + (\hat{\boldsymbol{F}}^T\boldsymbol{u}')_2^2}, \tag{3}$$

where $(\hat{\boldsymbol{F}}\boldsymbol{u})_j^2$ represents the square of the j'th entry of the vector $\hat{\boldsymbol{F}}\boldsymbol{u}$.

RANSAC is used as follows:

1. Eight putative correspondences are selected randomly and the fundamental matrix $\hat{\boldsymbol{F}}$ is estimated.
2. For each of the putative correspondences, if $d_S(\boldsymbol{u}, \boldsymbol{u}') < t_e$, the correspondence is counted.
3. Steps 1 and 2 are repeated for a desired number of iterations, and the set of correspondences with the largest count is taken to be the set of correct inliers.

3.4 *Optimal Fundamental Matrix Computation and Testing*

Once the largest set of inliers has been found, a epipolar test of the complete set of putative correspondences is performed. First, the set of inliers from RANSAC is used to compute the optimal LS estimate of the fundamental matrix. This is then used to select the putative correspondences from the original set that meet both the correlation threshold and the epipolar constraint using Eq. (3).

3.5 *Point Cloud Matching using Fused EO Image/Lidar Data*

At this point, it is possible to use the fused EO image and lidar data to compute the 3-D transformation from the second camera reference frame to the first reference frame. No disparity computation is required. Since each EO correspondence found previously has a 3-D point assigned to it, the 3-D points can then be used to find an estimate of the rigid body transformation from one lidar point cloud to the other.[36] The resulting transformation is found to be $(\hat{\boldsymbol{R}}, \hat{\boldsymbol{t}})$, where $\hat{\boldsymbol{R}}$ is the rotation matrix and $\hat{\boldsymbol{t}}$ is the translation vector from the second camera coordinate system to the first camera coordinate system.

3.6 *Improvement in Registration Exploiting 3-D Information*

Unfortunately, the epipolar constraint is necessary but not sufficient for corresponding points, since any point on an epipolar line (where the epipolar plane intersects the image planes) will satisfy the constraint. This is illustrated in Fig. 5, where erroneous correspondences that meet the epipolar constraint are marked as red circles and project on image 2 as red stars. Thus, it is possible that erroneous correspondences can be found if EO points in one image correlate highly with points in the other image and lie on the same epipolar line that the correct correspondence lies on.

A solution to the problem is to guide the selection of putative correspondences by using the results of the first attempt at registration to eliminate correspondences that are in error. This leads to an iterative solution: if the first iteration of the registration process described in Sects. 3.1–3.5 is reasonably close, it can be used to guide a better selection of correspondences, which can then be used to estimate the 3-D rigid transformation again.

3.6.1 *Epipolar constraint*

All of the putative correspondences have passed the epipolar constraint based on $\hat{\boldsymbol{F}}$ estimated from 2-D EO data. The test will be applied again, but with $\hat{\boldsymbol{F}}$ estimated from 3-D data. The fundamental matrix can be estimated using

$$\hat{\boldsymbol{F}} = \boldsymbol{K}^{-T}[\hat{t}_\times]\hat{\boldsymbol{R}}\boldsymbol{K}^{-1}, \tag{4}$$

where $\boldsymbol{K}$ is the EO camera calibration matrix (intrinsic parameters), and

$$[\hat{\boldsymbol{t}}_\times] = \begin{bmatrix} 0 & -\hat{z}_t & \hat{y}_t \\ \hat{z}_t & 0 & -\hat{x}_t \\ -\hat{y}_t & \hat{x}_t & 0 \end{bmatrix}, \tag{5}$$

which is constructed from $\hat{\boldsymbol{t}} = [\hat{x}_t \quad \hat{y}_t \quad \hat{z}_t]^T$. This new $\hat{\boldsymbol{F}}$ is used to test each remaining correspondence for the condition $\boldsymbol{u}'^T\hat{\boldsymbol{F}}\boldsymbol{u} < t_e$.

3.6.2 *Distance measures*

The 3-D information in the texel images is used to create a second restriction on correspondences remaining after the previous test. The 3-D point $\boldsymbol{x}'$ corresponding to the feature $\boldsymbol{u}'$ in texel image image 2 can be transformed into the coordinate system of texel image 1 using the relationship

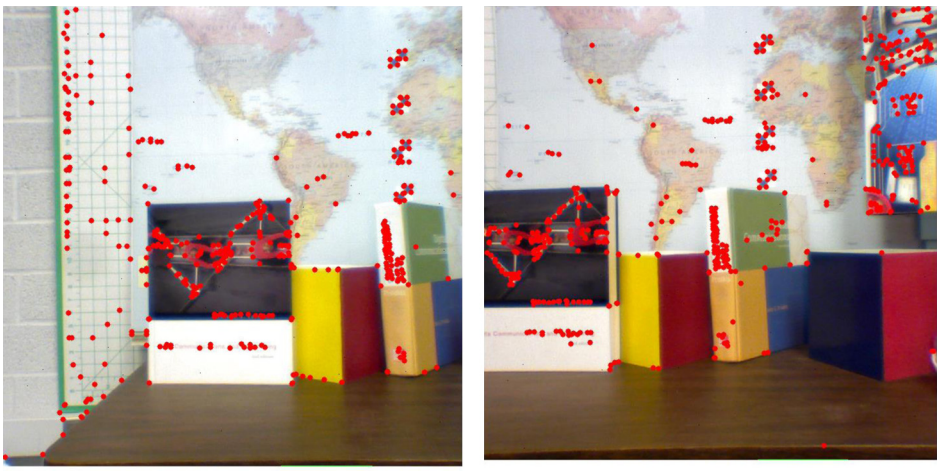

(a) (b)

Fig. 3 Examples of Harris features found in the (a) first and (b) second images and marked with red dots.

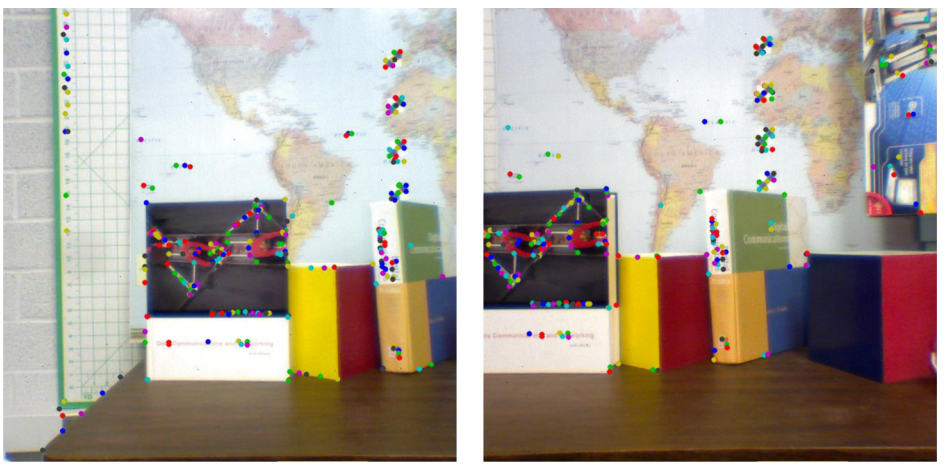

(a) (b)

Fig. 4 Examples of putative correspondences found in the (a) first and (b) second images and marked with corresponding colored dots.

$$\hat{\boldsymbol{x}} = [\hat{x} \quad \hat{y} \quad \hat{z}]^T = [\hat{\boldsymbol{R}} \quad \hat{\boldsymbol{t}}] \begin{bmatrix} \boldsymbol{x}' \\ 1 \end{bmatrix}. \tag{6}$$

If $(\hat{\boldsymbol{R}}, \hat{\boldsymbol{t}})$ and $(\boldsymbol{x}, \boldsymbol{x}')$ contain no error, then $\boldsymbol{x} = \hat{\boldsymbol{x}}$. Error in the estimates of $(\hat{\boldsymbol{R}}, \hat{\boldsymbol{t}})$ and the measurements of $\boldsymbol{x}$ and $\boldsymbol{x}'$ cause the pair $(\boldsymbol{x}, \hat{\boldsymbol{x}})$ to be unequal, as shown in Fig. 5. If the estimates of $(\hat{\boldsymbol{R}}, \hat{\boldsymbol{t}})$ are reasonably good, however, $\boldsymbol{x}$ and $\hat{\boldsymbol{x}}$ should be close to each other in 3-D space if $(\boldsymbol{u}, \boldsymbol{u}')$ is a correct correspondence.

The Euclidean distance between the 3-D points $(\boldsymbol{x}, \hat{\boldsymbol{x}})$ in the image 1 coordinate system is dependent on several factors related to the texel image taken in the image 2 coordinate system: the error in $(\hat{\boldsymbol{R}}, \hat{\boldsymbol{t}})$, sensor error, range to $\boldsymbol{x}'$, and the position of the detector on the lidar sensor array that measured the range to the point. The position of the detector can be measured as the azimuth and elevation of the detector relative to the principal ray of the texel camera, located at the center detector of the array at 0 deg in azimuth and elevation (boresight). This error is illustrated in Fig. 6(a). The blue ellipsoid represents a $1-\sigma$ error bound of 5 deg in attitude

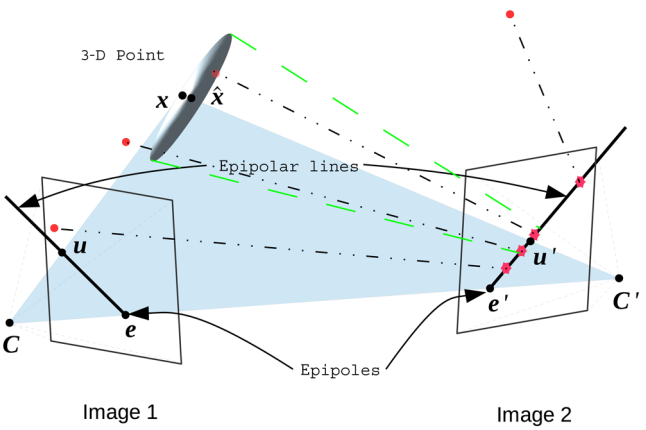

Fig. 5 Epipolar constraint required by projective geometry. The points $\boldsymbol{u}$ and $\boldsymbol{u}'$ represent corresponding image points projected from the three-dimensional (3-D) point $\boldsymbol{x}$, and the red points are erroneous correspondences to $\boldsymbol{u}$ satisfying the epipolar constraint. The center of projection of each camera is shown as $\boldsymbol{C}$ and $\boldsymbol{C}'$, respectively. The gray ellipsoid is discussed in Sec. 3.6.2.

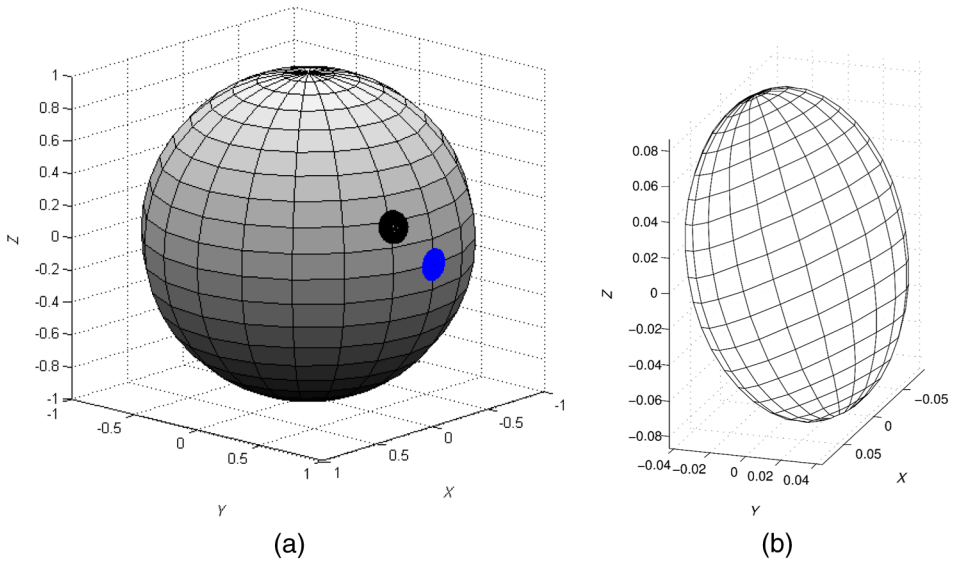

Fig. 6 Error ellipses in the image 2 coordinate system for $1-\sigma$ error of 5 deg in attitude knowledge, 1.5 cm in range, and 2 cm in position. (a) Ellipses on a constant range sphere at a range of 1 m from texel camera 2 and a boresight lidar direction (blue) and about 16.7 deg in azimuth and elevation (black). The *y*-axis is the principal ray (boresight) of the lidar sensor. (b) The 16.7-deg case translated to the origin to illustrate the error ellipse tilt. The boresight case is aligned with the axes (no tilt).

knowledge, 2 cm in position, and 1.5 cm in range at a range of 1 m from texel camera 2 and a boresight lidar measurement direction. The black ellipsoid is the error ellipse rotated to the position seen by the lidar detector at an azimuth and elevation of about 16.7 deg each, which corresponds to the detector in the lidar array with normalized image coordinates at (0.3, 0.3). The attitude, position, and range errors are assumed to be independent. The orientation of the error ellipsoid changes depending on the direction of the lidar measurement relative to the camera boresight, as illustrated in Fig. 6(b) for the off-boresight (black ellipsoid) case in Fig. 6(a). The tilt of error ellipse is evident.

The error ellipsoid relative to a 3-D point in the second texel image must be transformed into the first image coordinate system to test whether or not the two points are the same 3-D point. The result of this transformation is shown in Fig. 5, where the error ellipsoid for the point $\boldsymbol{x}'$ in the second coordinate system has been transformed to the first coordinate system (shown in gray). Note that the error ellipsoid also scales in size as the range changes, as indicated by the dashed green projection lines.[37] The 3-D point pair $(\boldsymbol{x}, \hat{\boldsymbol{x}})$ is indicated in the figure. The error ellipsoid represents the boundary in the image 1 coordinate system where the position of $\hat{\boldsymbol{x}}$ could be in error by $1-\sigma$.

The error ellipsoid can be constructed as follows. Assume the errors in $\hat{\boldsymbol{R}}$ and $\hat{\boldsymbol{t}}$ can be approximately described by a multivariate normal distribution with variances in the x, y, and z coordinates given by

$$\sigma_x^2 = r^2\tan^2(\sigma_\psi) + \sigma_{x_p}^2 \quad \sigma_y^2 = \sigma_r^2 + \sigma_{y_p}^2,$$
$$\sigma_z^2 = r^2\tan^2(\sigma_\phi) + \sigma_{z_p}^2, \tag{7}$$

where r is the range to the point $\boldsymbol{x}'$, σ_ψ, and σ_ϕ are standard deviations of the errors in the azimuth (rotations about the camera z axis) and elevation (rotations about the camera x axis) angles, σ_r is the range error, and $(\sigma_{x_p}, \sigma_{y_p}, \sigma_{z_p})$ is the camera position error. The tangent terms represent the motion of a point rotated at a range of r. A correlation matrix for the lidar boresight case is thus given by

$$\Sigma = \mathrm{Diag}(\sigma_x^2, \sigma_y^2, \sigma_z^2), \tag{8}$$

and the corresponding scatter matrix is rotated from boresight to the azimuth and elevation of the point $\boldsymbol{x}'$ using a rotation matrix $\boldsymbol{R}_\sigma$ describing the rotation, resulting in the scatter matrix

$$\Sigma_{\boldsymbol{R}_\sigma}^{-1} = \boldsymbol{R}_\sigma^T \Sigma^{-1} \boldsymbol{R}_\sigma. \tag{9}$$

Finally, the squared Mahalanobis distance between $\boldsymbol{x}$ and $\hat{\boldsymbol{x}}$ is found after rotating the scatter matrix into the coordinate system of image 1

$$d^2(\boldsymbol{x}, \hat{\boldsymbol{x}}) = [\boldsymbol{x} - \hat{\boldsymbol{x}}]^T \hat{\boldsymbol{R}}^T \Sigma_{\boldsymbol{R}_\sigma}^{-1} \hat{\boldsymbol{R}} [\boldsymbol{x} - \hat{\boldsymbol{x}}]. \tag{10}$$

If $d^2(\boldsymbol{x}, \hat{\boldsymbol{x}}) < 1$, the points are closer together than one standard deviation of the error, indicating that they likely are the same point. (Other thresholds can be used.)

The Mahalanobis distance is computed for each pair of correspondences in the set $(\boldsymbol{u}, \boldsymbol{u}_s')$. If none of the points in the set of $\boldsymbol{u}_s'$ passes the epipolar and distance tests, the $(\boldsymbol{u}, \boldsymbol{u}_s')$ correspondence set is removed. Otherwise, the correspondence in the set with the smallest Euclidean distance is retained.

After all of the correspondence sets are tested using the 3-D tests, the surviving correspondences are used to compute the updated estimate of $\hat{\boldsymbol{R}}$ and $\hat{\boldsymbol{t}}$.

An example of the results of this step is given in Fig. 7. The colored lines in the figure are the epipolar lines to which each inlier corresponds. Note that the correspondences are reduced to those that meet the correlation and epipolar constraint conditions in the two EO images and that also meet the Mahalanobis distance test with the 3-D lidar data.

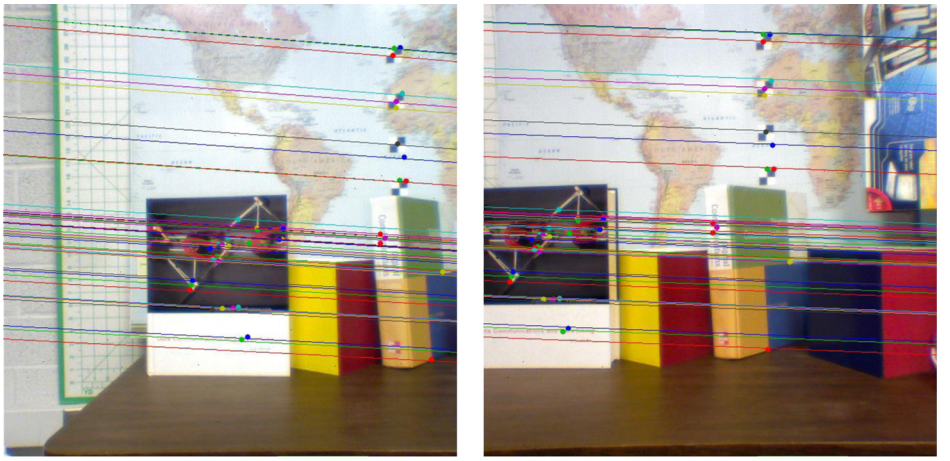

(a) (b)

Fig. 7 Examples of putative correspondences retained by 3-D epipolar and Mahalanobis distance test in the (a) first and (b) second images and marked with corresponding colored dots. The colored lines are the epipolar lines corresponding to the feature point.

4 Texel Image Registration Using Coarse Position and Attitude Information

In many applications, it is desirable to obtain GPS/IMU information available from small, low-cost microelectromechanical systems (MEMS). For example, these GPS/IMU sensors can be integrated with a miniaturized texel camera and used in a small unmanned aerial system (UAS) at a cost low enough to make the UAS accessible to a wide range of users.

The need for registration methods when only coarse position and attitude information is available is illustrated in Fig. 8, where the position and attitude of the camera for the second image contains 2 cm of position error (1.3% of the scene depth of 1.5 m) and 3 deg of attitude error (5.2%). Note that the blocks show an offset, and the background map is shifted. In a UAS application, a UAS flying at a 300-m altitude using a typical MEMS GPS/IMU would experience a maximum translation error of about 5 m (1.7%) and maximum attitude error corresponding to about 10.5 m (3.5%, assuming a rotation error of 2 deg), leading to registration errors of the type in Fig. 8. This reduces the accuracy of the registered 3-D image created by the UAS.

In addition to using the available GPS/IMU data, it is desirable to remove the dependence of the registration on image correlation. The method of Sec. 3 is limited in performance by a characteristic common to algorithms that rely on finding feature point correspondences in images using correlation. When the perspectives are widely separated, perspective distortion in the images causes the correlation between true correspondences to decrease to the point where correlation thresholds are not robust. An example of this problem is given in Fig. 9, where a potential Harris feature point is circled in green. Figure 9(a) is from a perspective in front of a checkered cube, and Fig. 9(b) is from above. It is evident that the image pixels around the point are significantly different and will lead to a low correlation value.

Fig. 8 Texel images with registration mismatch due to 2 cm of position error and 3-deg error in attitude, with a maximum scene depth of about 1.5 m. All texel image figures in this paper are taken from a 3-D viewing program.

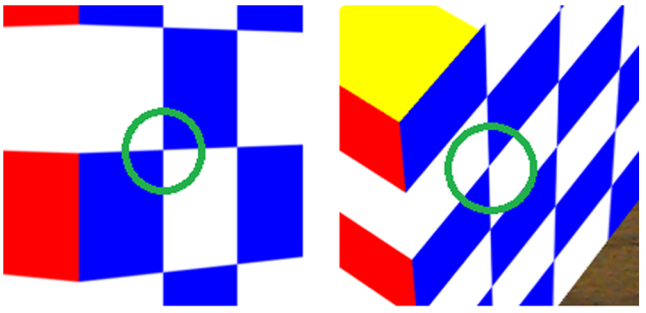

(a) (b)

Fig. 9 Examples of potential Harris feature points on a checkered cube from (a) a front perspective, and (b) a top perspective.

Algorithm 2 Automatic registration of texel images using position and attitude information.

1. Detect Harris features.
2. Estimate the fundamental matrix $\hat{\boldsymbol{F}}$ from $(\hat{\boldsymbol{R}}, \hat{\boldsymbol{t}})$ using (4).
3. Determine putative correspondences using $\hat{\boldsymbol{F}}$ and the position and attitude information $(\hat{\boldsymbol{R}}, \hat{\boldsymbol{t}})$:
   (a) Test each potential correspondence to determine that (3) holds.
   (b) If true, test that the Mahalanobis distance [Eq. (10)] between the corresponding 3-D points $(\boldsymbol{x}, \hat{\boldsymbol{x}})$ is below a threshold.
4. RANSAC using a fundamental matrix model and the epipolar constraint.
5. Estimate the optimal fundamental matrix $\hat{\boldsymbol{F}}$ and determine putative correspondences that meet the epipolar constraint to within a threshold.
6. Match point clouds using fused EO image/lidar data to create an estimate of the registration transformation $(\hat{\boldsymbol{R}}, \hat{\boldsymbol{t}})$.
7. Use the current estimate $(\hat{\boldsymbol{R}}, \hat{\boldsymbol{t}})$ and the fused EO image/lidar data to test putative correspondences and eliminate incorrect and many-to-one correspondences:
   (a) Estimate the fundamental matrix $\hat{\boldsymbol{F}}$ from $(\hat{\boldsymbol{R}}, \hat{\boldsymbol{t}})$ using (4).
   (b) Test each potential correspondence to determine that (3) holds.
   (c) If true, test that the Mahalanobis distance [Eq. (10)] between the corresponding 3-D points $\{(\boldsymbol{x}, \hat{\boldsymbol{x}}_s)\}$ is below a threshold. If all s in the set have a distance greater than the threshold, discard the set $\{(\boldsymbol{u}, \boldsymbol{u}'_s)\}$.
   (d) Select the correspondence with the minimum Euclidean distance out of the set of s correspondences.
8. Repeat step 6.

A second disadvantage of correlation-based methods is the computational cost. Correlation is performed using a window of image pixels around each feature point. Every point in the first image is correlated with every point in the second image, and a list of putative correspondences is created where the correlation value between points exceeds a threshold. For a list of N_1 features in the first image and N_2 features in the second image, the total number of correlations [Eq. (1)] that must be performed is $\mathcal{O}(N_1 N_2)$.

The method of Sec. 3 can be modified to register texel images with coarse GPS/IMU data. Image correlation around feature points appears in Algorithm 1 in step 2. GPS/IMU information will be used to replace the need for correlation in this step as given in Algorithm 2. The new steps 2 to 3 depend on an initial estimate of $(\hat{\boldsymbol{R}}, \hat{\boldsymbol{t}})$ given from the coarse GPS/IMU. It was observed that the RANSAC runs with many fewer iterations than in Algorithm 1 due to the epipolar test used in step 3a.

5 Registration Results

5.1 *Visual Performance*

The technique of Sec. 3 was applied to pairs of texel images of different scenes acquired from different positions and attitudes. The threshold t_e used for Eq. (3) during RANSAC was 0.5 pixels. For the tests in step 6 in the algorithm, the Sampson threshold t_e was increased to 5.0 pixels, and the standard deviations used in Eq. (7) were $\sigma_\psi = \sigma_\phi = 0.4$ deg, (corresponding to about 5 pixels in the EO images), and $\sigma_{x_p} = \sigma_{x_p} = \sigma_{x_p} = \sigma_r = 0.005$ m. These values were chosen based on the assumption that the registration up to this step was accurate within a few pixels in rotation and 0.5 cm in position. A Mahalanobis threshold of 2.0 was used.

A visual example of the results obtained using the texel images in Figs. 3–7 is illustrated in Fig. 10. Figures 10(a)–10(c) show the same images from a perspective view, revealing the 3-D nature of the images. Additional visualization of the 3-D is given by TINs in Figs. 10(d)–10(f). As can be seen in the figure, the registration of the two images is very good. The "seams" between the images occur next to the right textbook and halfway through the picture on the left textbook. These results are typical of results obtained using other texel image pairs.

One of the most difficult registration problems is the case where two flat planes need to be registered. If 3-D-only registration methods such as ICP are used, the registration process will often not converge or will converge to the wrong solution. In the noiseless case, any shift of the overlapping points will produce a minimum RMS registration error. For image-only registration and stereo 3-D reconstruction, it is possible that multiple points may satisfy (to within the threshold) the epipolar constraint as described in Sec. 3.6, resulting in erroneous correspondences. It is also difficult to compute stereo disparity if the images have large areas of constant color. An example of these problems is given in Fig. 11, where (a) and (b) are from texel images of a flat wall taken with a right shift in perspective. Note that several correspondences are incorrectly declared because multiple corners of the gray bars are highly correlated and lie close to the same epipolar line. Registration using these correspondences leads to an evident mismatch, as observed in the registration of the gray bar chart and the broken edges of the black squares on the right.

An example of the improvement in corresponding point selection by including step 6 in Algorithm 1 is given in Fig. 12. The erroneous correspondences have been removed, leaving a set of correct correspondences for computing a new transformation $(\hat{\boldsymbol{R}}, \hat{\boldsymbol{t}})$, which is then used to register the two texel images.

The advantage of the proposed method over ICP is illustrated with Fig. 13. This figure shows the registration achieved using ICP with point-to-point matching on the 3-D data only.[24] The registration is poor, with the red textbook aligned with the blue box. The difficulty with this approach is that ICP tries to find the LS registration estimate using all of the points presented to it; satisfactory results require some preprocessing or prior knowledge to determine which points in the two point clouds overlap. These images were successfully registered using the proposed method.

5.2 *Numerical Performance*

One of the major goals of this research is to create fused 3-D datasets that are not only visually pleasing, but that contain accurate distances between points in 3-D space. These 3-D images then can be used for scientific measurements of objects, or to improve the performance of object recognition

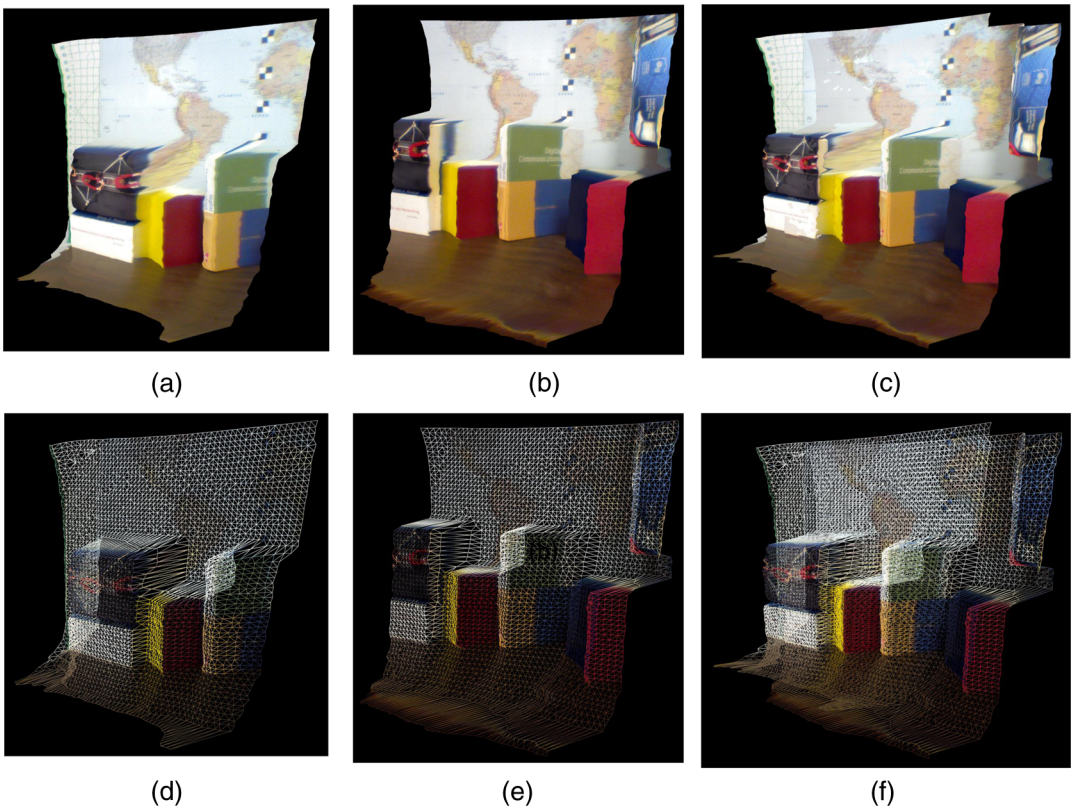

Fig. 10 Registered texel images and TINs from lidar measurements. All images taken from a perspective view. (a) First texel image. (b) Second texel image. (c) Registered texel image. (d) First image TIN. (e) Second image TIN. (f) Registered image TIN.

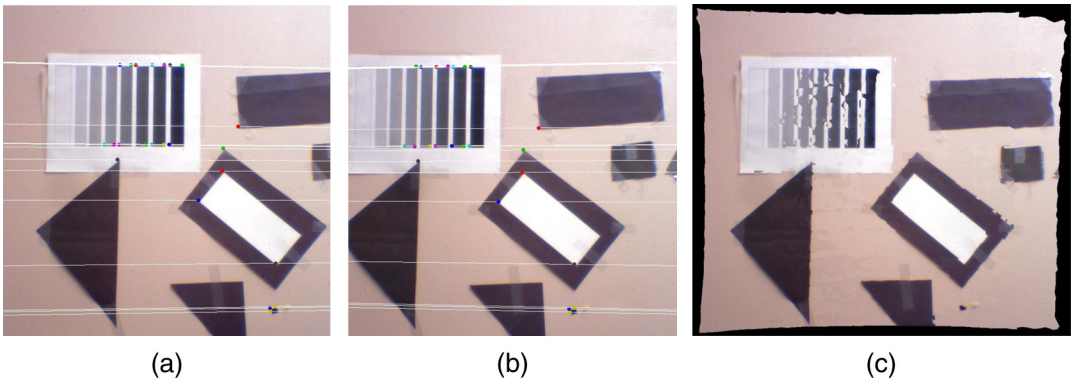

Fig. 11 Examples of erroneous correspondences passing the epipolar constraint and the resulting registered texel image. (a) First EO image. (b) Second EO image. (c) Registered texel image. Correspondences are marked with the same color dot.

algorithms. One measure of registration quality is the mean-squared error (MSE) between corresponding 3-D points in the registered dataset. The MSE is given in m^2. For the results that follow, a texel image of the scene served as ground truth. Since the calibration of the camera gives 1-sigma 3-D position errors of about 3 mm,[31] it was deemed accurate enough.

To quantify the performance of the algorithms, five scenes were captured and registered. The algorithm parameters used are given in Sec. 5.1. For the tests for Algorithm 2, a translation error of 3 cm and rotation error of 3 deg were artificially added. The MSE for the proposed algorithms was recorded after the first computation of $(\hat{\boldsymbol{R}}, \hat{\boldsymbol{t}})$, and the final MSE was computed after "bad" correspondences were removed using the Sampson distance test [using $\hat{\boldsymbol{F}}$ from $(\hat{\boldsymbol{R}}, \hat{\boldsymbol{t}})$] and the Mahalanobis distance test, and recomputing $(\hat{\boldsymbol{R}}, \hat{\boldsymbol{t}})$. The MSE for the 3-D ICP method was also recorded. MATLAB code for the ICP method used was provided by Tang,[38] with the ICP tolerance parameter set to 2 cm. The results are given in Table 2. The final estimate resulted in a reduction in MSE of an order of magnitude for Algorithm 1, and nearly half for Algorithm 2 (which uses no correlation to find corresponding points). The MSE for the ICP registration is significantly larger than that for the

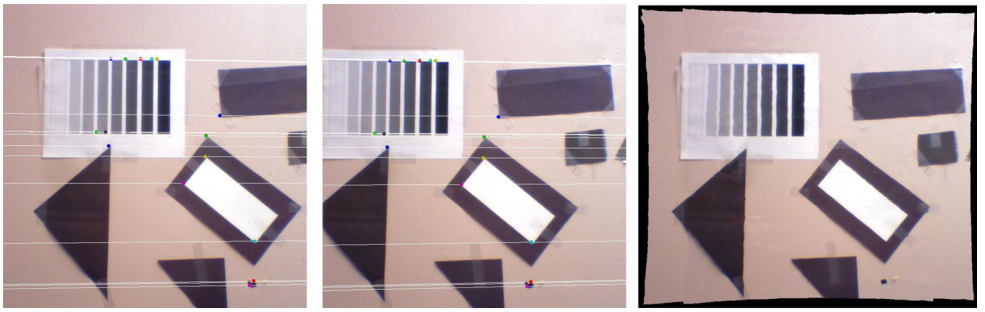

Fig. 12 Improved correspondences after using step 6 in Algorithm 1 and the resulting registered texel image. (a) First EO image. (b) Second EO image. (c) Registered texel image.

Fig. 13 Registration result achieved using iterated closest point on the lidar point cloud only. The blue box in the right image is clearly misregistered with the blue box in the left image.

proposed methods. This is because in these cases the ICP method failed to produce a good registration.

An additional case was captured where the perspective difference between the texel images was larger—the second texel image was taken from a position 13 cm to the left and 2 cm closer, with a rotation of 10-deg clockwise. As before, a translation error of 3 cm and rotation error of 3 deg were artificially added. The registration results are presented as Image pair 6. Note that Algorithm 2 performs better than Algorithm 1. This is because the correlation step was unable to find as many correspondences as the initialization with coarse GPS/IMU data.

Another measurement of the accuracy of the algorithms was taken by registering two texel images of a scene and then measuring the 3-D distance across the registered scene between 3-D points in the first texel image and 3-D points in the second texel image. The points chosen were not image correspondences, but arbitrary 3-D points in the scene. These distances were compared to the ground truth distances between these points as measured in a single-texel image as mentioned above. This measures the quality of the registration for use in applications where the dimension of objects in the registered scene are of interest, and the objects extend across the registered images. Points which were distributed throughout the scene were chosen, resulting in 72 unique

Table 2 Mean-squared error (MSE) between corresponding points in the registered dataset.

	Corresponding point MSE				
	Algorithm 1		Algorithm 2		
Dataset	Step 5	Step 6	Step 6	Step 7	ICP
Image pair 1	1.079×10^{-3}	1.715×10^{-5}	3.063×10^{-5}	2.132×10^{-5}	9.900×10^{-3}
Image pair 2	3.739×10^{-4}	2.051×10^{-5}	9.694×10^{-5}	5.408×10^{-5}	8.800×10^{-3}
Image pair 3	1.890×10^{-4}	1.290×10^{-5}	2.149×10^{-5}	1.484×10^{-5}	7.600×10^{-3}
Image pair 4	1.999×10^{-5}	1.281×10^{-5}	8.720×10^{-5}	4.479×10^{-5}	7.900×10^{-3}
Image pair 5	3.042×10^{-4}	2.942×10^{-5}	4.744×10^{-5}	3.132×10^{-5}	8.600×10^{-3}
Average	3.932×10^{-4}	1.856×10^{-5}	5.674×10^{-5}	3.327×10^{-5}	8.560×10^{-3}
Corresponding point error—poor correlation					
Image pair 6	2.948×10^{-3}	5.318×10^{-4}	3.032×10^{-4}	4.074×10^{-5}	1.180×10^{-2}

Table 3 Error means and standard deviations (in meters) between corresponding distances in the ground truth and registered datasets.

	Corresponding distance error					
	Algorithm 1		Algorithm 2		ICP	
Dataset	μ	σ	μ	σ	μ	σ
Image pair 1	-1.300×10^{-3}	1.240×10^{-2}	6.660×10^{-4}	2.900×10^{-3}	-5.087×10^{-2}	1.260×10^{-1}
Image pair 2	-1.000×10^{-3}	3.700×10^{-3}	6.313×10^{-4}	3.900×10^{-3}	-3.850×10^{-2}	1.026×10^{-1}
Image pair 3	4.591×10^{-4}	3.600×10^{-3}	-1.900×10^{-3}	2.700×10^{-3}	-3.179×10^{-2}	7.995×10^{-2}
Image pair 4	-1.200×10^{-3}	1.900×10^{-3}	-1.800×10^{-3}	1.800×10^{-3}	-3.054×10^{-2}	6.796×10^{-2}
Image pair 5	2.993×10^{-4}	2.700×10^{-3}	6.304×10^{-4}	2.300×10^{-3}	-1.428×10^{-2}	6.429×10^{-2}
Average	-5.483×10^{-4}	4.860×10^{-3}	-3.545×10^{-4}	2.720×10^{-3}	-3.320×10^{-2}	8.816×10^{-2}
	Corresponding distance error—poor correlation					
Image pair 6	-5.10×10^{-3}	1.410×10^{-2}	-1.50×10^{-3}	6.90×10^{-3}	-3.720×10^{-2}	6.50×10^{-2}

3-D distances between the points. The distances between these points in the ground truth texel image were computed, and the corresponding distances between the same scene points in the ground truth texel image and the registered texel image 2 were compared by finding the error between the ground truth and registered distances. The results are given in Table 3.

These results show that both proposed methods result in significantly better registration than the ICP method, when the measurement of distances between points across the registered dataset is important. As observed in Table 2, the errors for Image pair 6 are greater for Algorithm 1 than Algorithm 2.

6 Conclusion

The method described in this paper has been shown to perform very well in registering textured 3-D point clouds (texel images) to create a 3-D mosaic of two images. If multiple texel images from different perspectives surrounding a scene are used, it is possible to create a true 3-D image of the scene.

Registration is based on the unique properties of texel images. Since the EO image is fused to the 3-D lidar measurements at the sensor level, no 2-D-to-3-D registration and the resulting additional error is introduced into the process. In addition, the registration of the texel images uses both the EO image and the 3-D measurements. This allows for iterative improvement of the registration because the images must satisfy both the properties of projective geometry and 3-D rigid transformation. Also, since measured 3-D information is used in the registration, this method does not require decomposition of the fundamental matrix to find the 3-D transformation and resolution of the scale ambiguity often faced in 2-D image-only methods. As shown in the experiments, the proposed methods can also avoid the poor registration that can result from ICP using only 3-D data.

Both registration with no *a priori* knowledge, and with coarse knowledge of position and attitude were presented. Registration was successful with both methods. It was shown that with coarse position and attitude information, it is unnecessary to depend on image correlation to find initial putative correspondences, enabling registration of texel images of widely different perspectives, and avoiding the computational requirements for multiple correlation calculations.

There are many new and exciting areas for ongoing research in texel image registration. For example, the robustness of the techniques presented here must be studied further. Although not a goal of this study, the selection of feature points in low-contrast imagery must be improved. In addition, the sensitivity of the algorithm to the thresholds for the Harris detector, correlation threshold, t_e, and the Mahalanobis distance must be studied. It was also observed that Algorithm 2 was sensitive to the condition where Harris points were clustered in the images. Finally, the fused-dataset nature of texel images also opens the possibility of image and shape super-resolution techniques to improve both the resolution of the EO textures and the density and accuracy of the 3-D data upon which the textures are applied.

References

1. S. E. Budge et al., "People matching for transportation planning using texel camera data for sequential estimation," *IEEE Trans. Hum.-Mach. Syst.* **43**, 619–629 (2013).
2. M. D. Elstrom and P. W. Smith, "Stereo-based registration of multi-sensor imagery for enhanced visualization of remote environments," in *Proc. IEEE Int. Conf. Robotics and Automation*, Vol. 3, pp. 1948–1953, IEEE, New York, NY (1999).
3. U. Hahne and M. Alexa, "Combining Time-Of-Flight depth and stereo images without accurate extrinsic calibration," *Int. J. Intelligent Systems Technologies and Applications* **5**(3/4), 325–333 (2008).
4. J. Zhang et al., "High quality depth maps from stereo matching and ToF camera," in *2011 International Conf. of Soft Computing and Pattern Recognition (SoCPaR)*, pp. 68–72 (2011).
5. I. Stamos and P. K. Allen, "Integration of range and image sensing for photorealistic 3D modeling," in *Proc. IEEE Int. Conf. on Robotics and Automation*, pp. 1435–1440, IEEE, New York, NY (2000).
6. R. Kurazume et al., "Simultaneous 2D images and 3D geometric model registration for texture mapping utilizing reflectance attribute," in *The 5th Asian Conf. on Computer Vision*, pp. 454–461, Asian Federation of Computer Vision Societies (AFCV) (2002).
7. P. Dias et al., "Automatic registration of laser reflectance and colour intensity images for 3D reconstruction," *Rob. Auton. Syst.* **39**(3–4), 157–168 (2002).
8. F. Deng et al., "Registration of LIDAR and optical images using multiple geometric features," *Proc. SPIE* **6787**, 678714 (2007).

9. L. Borgeat et al., "A framework for the registration of color images with 3D models," in *Proc. IEEE Int. Conf. Image Processing (ICIP)*, pp. 69–72, IEEE, New York, NY (2009).
10. K. Umeda, G. Godin, and M. Rioux, "Registration of range and color images using gradient constraints and range intensity images," in *Proc. Int. Conf. Pattern Recogition*, Vol. 3, pp. 12–15, IEEE (2004).
11. F. Deng, S. Li, and G. Su, "Mutual information based registration of LIDAR and optical images," *Proc. SPIE* **6752**, 675247 (2007).
12. D. Scharstein and R. Szeliski, "A taxonomy and evaluation of dense two-frame stereo correspondence algorithms," *Int. J. Comp. Vision* **47**, 7–42 (2002).
13. R. Hartley and A. Zisserman, *Multiple View Geometry in Computer Vision*, second ed., Cambridge University Press, Cambridge, UK (2003).
14. F. Remondino et al., "Turning images into 3-D models," *IEEE Signal Process. Mag.* **25**(4), 55–65 (2008).
15. B. Zitova and J. Flusser, "Image registration methods: a survey," *Image Vis. Comput.* **21**, 977–1000 (2003).
16. A. Baumberg, "Reliable feature matching across widely separated views," in *Proc. IEEE Conf. Computer Vision and Pattern Recogition (CVPR)*, Vol. 1, pp. 774–781 (2000).
17. T. Tuytelaars and L. Van Gool, "Matching widely separated views based on affine invariant regions," *Int. J. Comput. Vision* **59**(1), 61–85 (2004).
18. M. Brown and D. G. Lowe, "Automatic panoramic image stitching using invariant features," *Int. J. Comput. Vision* **74**(1), 59–73 (2007).
19. T. Lindeberg, "Scale selection properties of generalized scale-space interest point detectors," *J. Math. Imaging Vision* **46**(2), 177–210 (2013).
20. M. S. Yasein and P. Agathoklis, "A robust, feature-based algorithm for aerial image registration," in *IEEE Int. Symp. on Industrial Electronics*, pp. 1731–1736, IEEE (2007).
21. J. Liang and Y. Zhou, "Vector features for image matching and image registration," in *Fifth Int. Conf. on Graphic and Image Proc. (ICGIP 2013)*, Vol. 9069, 906918, SPIE (2014).
22. S. E. Budge and X. Xie, "Improved registration for 3D image creation using multiple texel images and incorporating low-cost GPS/INS measurements," *Proc. SPIE*, **9080**, 90800O (2014).
23. P. J. Besl and N. D. McKay, "A method for registration of 3-D shapes," *IEEE Trans. Pattern Anal. Mach. Intell.* **14**(2), 239–256 (1992).
24. S. Rusinkiewicz and M. Levoy, "Efficient variants of the ICP algorithm," in *Third Int. Conf. on 3-D Digital Imaging and Modeling*, pp. 145–152, IEEE (2001).
25. K. Nishino and K. Ikeuchi, "Robust simultaneous registration of multiple range images," in *Proc. 5th Asian Conf. Computer Vision*, pp. 454–461, Asian Federation of Computer Vision Societies (AFCV) (2002).
26. A. Grün and D. Akca, "Least squares 3D surface matching," in *ASPRS 2005 Annual Conf., (on CDROM)*, ASPRS, Baltimore, Maryland (2005).
27. S. E. Budge and N. Badamikar, "Automatic registration of multiple texel images (fused lidar/digital imagery) for 3D image creation," *Proc. SPIE* **8731**, 873107 (2013).
28. R. T. Pack, P. Israelsen, and K. Sealy, "A co-boresighted synchronized ladar/EO imager for creating 3D images of dynamic scenes," *Proc. SPIE* **5791**, 42–50 (2005).
29. B. M. Boldt et al., "A handheld texel camera for acquiring near-instantaneous 3D images," in *Proc. Asilomar Conf. Signals, Systems, and Computers*, pp. 953–957, IEEE (2007).
30. R. T. Pack et al., "Eyesafe LADAR test-bed with coaxial color imager," *Proc. SPIE* **7323**, 732303 (2009).
31. S. E. Budge and N. S. Badamikar, "Calibration method for texel images created from fused lidar and digital camera images," *Opt. Eng.* **52**(10), 103101 (2013).
32. C. Harris and M. Stephens, "A combined corner and edge detector," in *Proc. of Fourth Alvey Vision Conf.*, pp. 147–151, University of Sheffield Printing Office, UK (1988).
33. M. A. Fischler and R. C. Bolles, "Random sample consensus: a paradigm for model fitting with applications to image analysis and automated cartography," *Commun. ACM* **24**(6), 381–395 (1981).
34. R. I. Hartley, "In defense of the eight-point algorithm," *IEEE Trans. Pattern Anal. Mach. Intell.* **19**(6), 580–593 (1997).
35. C. L. Feng and Y. S. Hung, "A robust method for estimating the fundamental matrix," in *Proc. VIIth Digital Image Computing: Techniques and Applications*, C. Sun et al., Eds., pp. 633–642, Csiro Publishing, Australia (2003).
36. D. W. Eggert, A. Lorusso, and R. B. Fisher, "Estimating 3-D rigid body transformations: a comparison of four major algorithms," *Mach. Vision Appl.* **9**(5/6), 272–290 (1997).
37. K. von Niederhäusern, "Automatic merging of lidar three-dimensional point clouds using inertial navigation systems and global positioning systems data," Master's Thesis, Utah State University (2007).
38. R. Tang, "The simple GUI program for point clouds registration," http://www.mathworks.com/matlabcentral/fileexchange/35019-the-simple-gui-program-for-point-clouds-registration/content/PCM/icp.m (2012).

Scott E. Budge received his BS, MS, and PhD degrees in electrical engineering from Brigham Young University in 1984, 1985, and 1990, respectively. He joined the faculty at Utah State University in January of 1989, where he has been involved in research into image data compression algorithms for transmission systems and space-based observation platforms. His current work involves research on methods for exploitation of full-waveform LADAR and EO images for 3-D image applications. He is also involved in the development of high-performance image processing algorithms designed for implementation in hardware and VLSI systems.

Neeraj S. Badamikar received his Bachelor of Engineering degree in electronics and telecommunication in 2011 from Vishwakarma Institute of Information Technology, Pune. He is pursuing his Master of Science degree in electrical engineering from Utah State University, USA. His current research involves automatic registration of multiple texel images to form a combined texel image.

Xuan Xie received his Bachelor of Engineering degree in communication engineering in 2005 from the University of Electronic Science and Technology of China, Chengdu, China, and his Master of Engineering degree in software engineering in 2009, from Tsinghua University, Beijing, China. He is pursuing his PhD degree in electrical engineering from Utah State University, USA. His current research involves registration of texel images using a lidar camera and object recognition using a lidar camera.